



On Performance and fouling of thin film composite hollow Fiber membranes using polycarbonate/polyvinylchloride as porous substrates for forward osmosis applications

Z. Alihemati^a, S.A. Hashemifard^{a,*}, T. Matsuura^{b,c}, A.F. Ismail^{b,*}

^a Sustainable Membrane Technology Research Group (SMTRG), Faculty of Petroleum, Gas and Petrochemical Engineering(FPGPE), Persian Gulf University (PGU), P.O. Box 75169-13798, Bushehr, Iran

^b Advanced Membrane Technology Research Centre (AMTEC), Universiti Teknologi Malaysia, 81310 UTM Skudai, Johor Darul Ta'zim, Malaysia

^c Department of Chemical and Biological Engineering, University of Ottawa, 161 Louis Pasteur St., Ottawa, ON K1N 6N5, Canada

ARTICLE INFO

Editor: Despo Kassinos

Keywords:

Polycarbonate
Thin-film composite
Polyvinylchloride
Forward osmosis
Hollow fiber membranes

ABSTRACT

In this study, thin-film composite (TFC) hollow fibers (HFs) were fabricated by an in-situ coating of polyamide layer on the lumen side of PVC/PC blend substrates for desalination by forward osmosis (FO). Particularly, the substrate HFs were spun at two air gap distances of 2 and 6 cm, to investigate the effect of the air-gap distance on the FO performance. The substrate HFs were characterized by pure water flux measurement, FESEM, and gas permeability test. The Interfacial polymerization (IP) method was then utilized for coating polyamide (PA) layer on the lumen surface of the substrate to fabricate TFC HFs. The TFC HFs so fabricated were also characterized by FESEM, before their FO performance was tested. Furthermore, the effect of HF length on the FO flux was investigated. The results showed that the novel TFC HFs exhibited good FO performance. The longer the air gap distance, the better becomes the FO performance in terms of simultaneous water flux and alginate fouling resistance, while the effect of the HF length remains a controversial issue.

1. Introduction

Water scarcity is considered as one of the most crucial issues in the world [1,2] which needs to be addressed urgently by exploring alternative resources, such as wastewater reclamation and seawater desalination [3–7]. Nanofiltration (NF), Forward osmosis (FO), and reverse osmosis (RO) processes are membrane-based separation technologies that are currently employed for supplying freshwater from wastewater and saline water [8]. RO is regarded as the most commonly used commercial membrane process for water treatment. However, severe membrane fouling [9], and concentrated brine exiting from the process remain its serious challenges. To produce clean water, typical membrane processes usually use hydraulic pressure as the driven force for separation. However, FO uses osmosis through a semi-permeable membrane to extract pure water from a low salinity solution (feed solution) to a draw solution as a high salinity one [10–12]. Therefore, FO process does not require high-pressure pumps. Nevertheless, challenges such as high reverse salt flux, low water flux, fouling [13] and difficulty to recover draw solution have impeded commercializing FO technology [14].

Membrane properties largely control the FO process performance. Therefore, it is imperative to design and fabricate membranes that are most suitable for FO. Among the membranes applied in the osmosis process, thin film composite (TFC) membranes have so far been most extensively used for the FO process [15–17]. TFC membranes consist of a porous substrate and a dense active layer coated via the IP method onto the top surface of the porous substrate [18–21]. Indeed, applying a composite structure comprising a porous substrate of inexpensive material and a thin and dense active layer can decrease the overall membrane material cost. Also, the properties of the porous substrate and the active layer can be optimized individually [22]. TFC-FO membranes can be classified geometrically into two forms: (i) flat sheet and (ii) hollow fiber (HF) membranes [23]. HF membranes have some advantages over flat sheet membranes [24,25], such as self-supported mechanical properties, enabling the higher effective surface area in a module [26], and also easiness of scaling-up. In addition, HF can offer novel flow patterns required for FO process [27–30]. Overall, for large-scale applications, HF membranes could be more economical [31]. Despite these advantages, the fabrication of FO hollow fiber membranes faces several

* Corresponding authors.

E-mail addresses: salhashemifard@pgu.ac.ir (S.A. Hashemifard), salhashemifard@pgu.ac.ir (A.F. Ismail).

<https://doi.org/10.1016/j.jece.2021.106828>

Received 8 September 2021; Received in revised form 12 November 2021; Accepted 14 November 2021

Available online 27 November 2021

2213-3437/© 2021 Elsevier Ltd. All rights reserved.

Table 1
Dope composition and fabrication conditions of prepared HF substrates.

Parameters	Remarks
Dope composition (wt%): PC/PVC/PEG400/NMP	8.5/8.5/4/79
Bore fluid	DI water
Dope fluid flow rate (ml/min)	2
Bore fluid flow rate (ml/min)	4
Spinneret OD/ID, mm	0.8/1.6
External coagulant bath	Tap water
Coagulation bath temperature	Room temperature

challenges. They are related to the limitation of suitable materials (hydrophilic and mechanically robust) for the substrate hollow fibers, i.e., necessity to improve the phase separation methods for the fabrication of HFs with high permeation properties and good mechanical properties [32]. Numerous studies have been performed on the hollow fiber membranes in the FO process. In these studies, polymers such as PES [23,29,33–35], sulfonated polyphenylene sulfone [30] Matrimid [27], PAN [36], and Polyketone [37] have been used as substrates. In some cases, the active layer is made on the inner surface and in the others on the outer surface of the membrane. In addition, the effect of various parameters on membrane properties and performance has been discussed. Zhong et al. [30] studied the effect of the degree of sulfonation of polyphenylene oxide on the morphology of HF substrate and its impact on the performance of the inner selective skin layer. Luo et al. [27] spun Matrimid HF substrate with a three-needle blossom spinneret to fabricate inner selective membrane and reported that their HF had superior durability with respect to those spun by a simple spinneret, enabling easier washing and long-term operation. Ren et al. [36] prepared PAN with outer selective HF membrane and studied the bore fluid effect on the substrate structure and membrane performance. Shibuya et al. [37] fabricated TFC outer selective HF membranes with Polyketone substrates. They investigated the effect of diameters and thicknesses of substrates on the membrane performance [37].

In the present study, a thin-film composite of hollow fiber membrane was fabricated for use in a forward osmosis process having a PVC/PC substrate and an inner-selective polyamide substrate. PVC polymer is one of the economical membrane materials that have been widely used to make ultrafiltration membranes. This polymer is hydrophobic hence it has been attempted to enhance the hydrophilicity of PVC membrane [38]. As a practical method, one can blend it with a hydrophilic polymer like PC due to the presence of carbonate group in the PC chains. The good compatibility between PC and PVC was demonstrated by Behboudi et al. [39]. In this study, the effect of various parameters on membrane performance was discussed. During the substrate construction stage, the effect of air gap on the structure of the substrate surface, including surface pore size and the effective surface porosity, were investigated. The substrate surface have a great impact on the characteristics of the polyamide active layer and the formation of a defect free active layer. Therefore, the effect of substrate surface characteristics on membrane structural parameter, membrane performance in the process of forward osmosis and membrane fouling with sodium alginate feed were discussed. Also, after fabricating the membrane with the optimal substrate, the effect of fiber length on membrane performance in the forward osmosis process was discussed. Furthermore, to the best of authors' knowledge, no such studies have been addressed, where PVC/PC blend was used as a substrate for fabricating the TFC hollow fiber FO membrane. Moreover, in only very few investigations the effects of the surface porosity of the porous substrate membrane on the structural parameter and FO performance of the TFC prepared membrane have been investigated.

2. Experimental

2.1. Materials and chemicals

Polyvinyl chloride (MW=90000, Arvand Petrochemical Company), polycarbonate (MW=90000, Khuzestan Petrochemical Company) were used as substrate materials. 1-methyl-2-pyrrolidinone (NMP) (>99.5%) as a solvent and Polyethylene glycol (PEG) 400 as a pore former were applied for preparation of membrane substrates. 1,3-phenylenediamine (MPD) (>99%), sodium dodecyl sulfate (SDS), n-hexane (>99%) and 1,3,5-benzenetricarbonyl trichloride (TMC) (>98%) supplied by Merck were used for fabricating inner polyamide (PA) selective and dense layer of TFC membranes.

2.2. Fabrication of hollow fiber membrane substrates

In this study, a dry-jet wet spinning technique was used to prepare the HF substrate membranes [23]. Table 1 summarizes the dope composition as well as the spinning conditions. To prepare the dope solution, a predetermined amount of polymer blend (0.5%wt PVC in PC) was dissolved in NMP/PEG solution at 40 °C for 24 h under magnetic stirring. Then, the homogeneous solution was degassed overnight. PEG was used for the formation of a sponge-like porous structure. The polymer solution so prepared was injected the spinneret applying a syringe pump with a fixed flow rate. The bore fluid was also fed into the spinneret with another syringe pump at a constant flow rate. After being extruded from the spinneret, the as-spun HF entered into the coagulation bath after traveling the air gaps of either 2 and 6 cm. Thus, depending on the air gap distance, the HFs are called HF-2 or HF-6. HFs were further kept immersed in tap water for two days to ensure the release of the remaining solvent. The coagulation bath was refreshed with fresh water from time to time to perform a good solvent exchange. The HFs were then divided into two groups. The first one was kept in the water bath for another day and then dried in the ambient condition for three days (They were used for gas permeation testing.). The other one was kept in a 50 wt% glycerol solution in water for one day, and then dried for three days to avoid the shrinkage of membrane pores. The latter one was used for pure water permeation and FO tests. Two kinds of stainless-steel housings with a diameter of 0.013 m and lengths of 0.15 and 0.25 m were used. In all performance tests, a module with a hollow fiber length of 0.1 m was used and for investigating the fiber length effect on membrane performance it was compared with the module with 0.19 m fiber length. Each module contained five membranes.

2.3. Formation of inner-selective active layer

The TFC membranes were fabricated by coating a PA layer on the lumen side of the HF substrates via IP using the two monomers, MPD and TMC, as described earlier [29,33,34,40,41]. Fig. 1 demonstrates the stepwise IP process applied onto the inner surface of the HF substrates. First, five post-treated HF substrates without defect were put into a module and then both ends were glued to the module with epoxy resin carefully without deforming the HFs. Then, the module was immersed in Deionized (DI) water for 12 h, followed by purging water in the HF lumen by sweeping air for 1 min. The module was then held vertically and the aqueous solution containing 2 wt% MPD and 0.1 wt% SDS was pumped by a peristaltic pump with a flow rate of 4.2 ml/min for 5 min into the lumen of the HF from bottom to top. Excess MPD solution in the lumen was purged by a sweeping air for 5 min. Afterward, TMC (0.15 wt %) dissolved in N-hexane was injected into the HF lumen side with a constant flow rate of ~2.5 ml/min per 5 min. Then, the residual hexane solution was purged by a sweeping air for 30 s. The membrane module was left in the atmosphere for 10 min before being cured in an oven for 15 min at 60 °C. The polyamide active layer is formed by the reaction of two amino and carboxylic monomers during condensation polymerization. A condensation reaction occurs between an organic base (such as

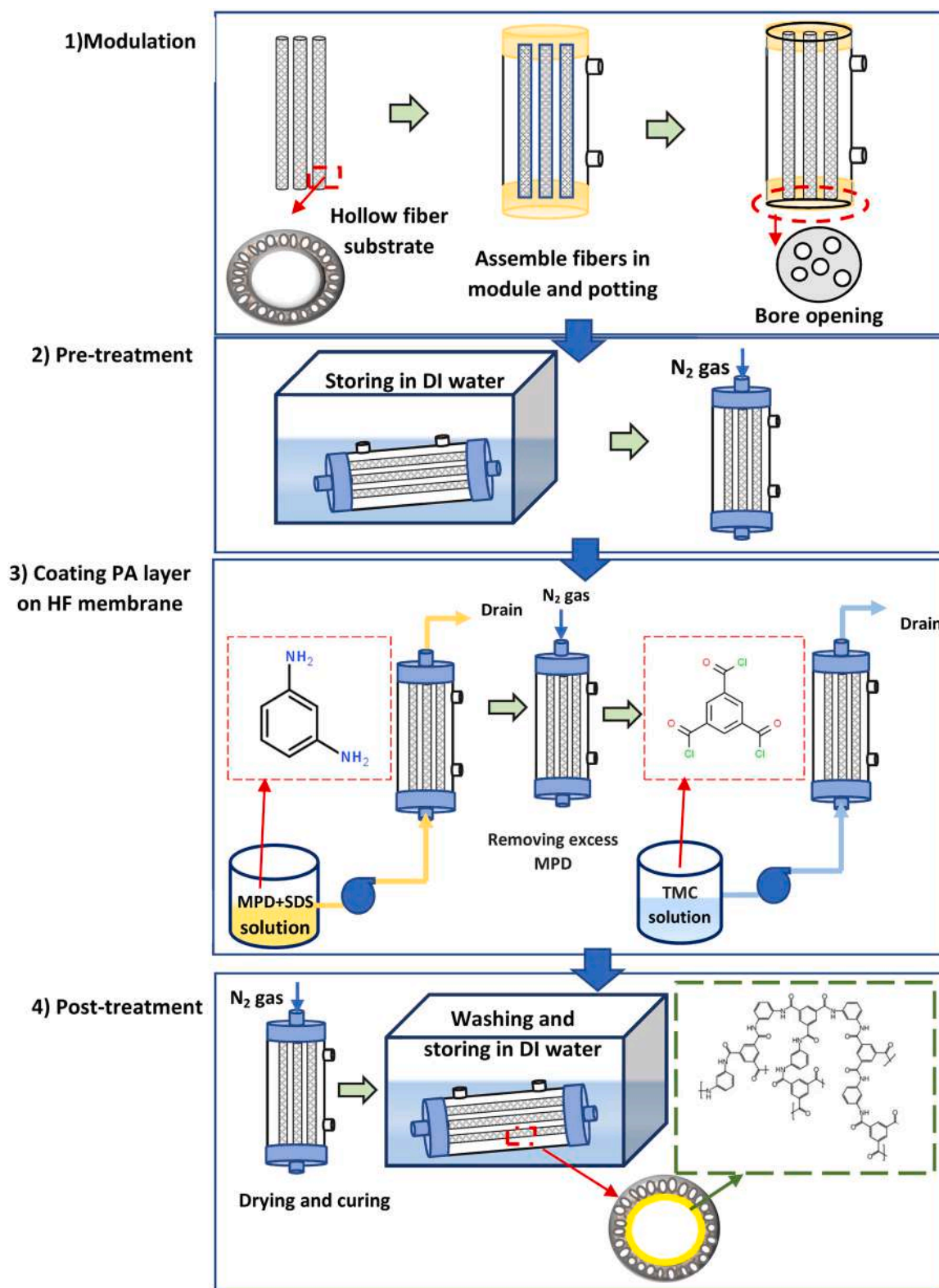


Fig. 1. The stepwise process of fabricating active layer on the lumen side of the HF.

an alcohol or an amine) and an organic acid (such as a carboxylic acid), accompanied by the release of a small molecule (usually water). The MPD monomer consists of a benzene ring and two amine groups (-NH₂). TMC also possesses one benzene group and three acyl halide groups (-COCl). As a result, after reacting the two monomers, a molecule of hydrochloric acid (HCl) is formed and a cross-linked active layer is

obtained [42,43]. Heat curing results in more crosslinking and better salt retention. Heat treatment is often used to remove the residual organic solvent from the solution, thereby increasing crosslinking by the reaction of unreacted amines and carboxyl groups [44].

Then, the modules were left overnight in room condition and then washed with deionized water and finally kept immersed in DI water

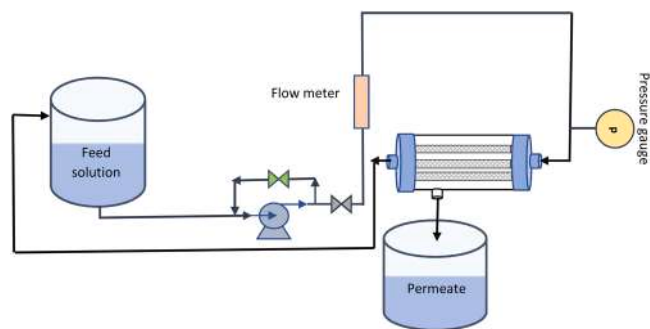


Fig. 2. A lab scale RO set up for determining pure water flux.

before the characterization and the performance test.

2.4. Membrane characterizations

2.4.1. Morphology of the HF membrane

The surface (inner and outer surface), and cross-sectional images of the HF membrane were captured by a scanning electron microscope (FESEM; MIRA III, Tescan). To observe the cross-section of the membranes, the HF samples were broken after chilling in liquid nitrogen. All HF samples were placed on a conductive carbon tape and a thin layer of gold was sputtered to coat the membrane samples, preventing the accumulation of charge before imaging.

2.4.2. Membrane porosity

To determine the overall HF membrane porosity (ϵ_b) of the prepared substrates, a Gravimetric method was applied as presented by Eq.(1), where w_{wet} and w_{dry} are the wet and dry membrane weight, respectively. For weighing w_{wet} , three fibers were taken out from water bath. Then excess water was removed from the outer and inner surface of the HFs carefully by paper tissue and mouth blowing inside the hollow fibers, respectively. ρ_p and ρ_{H_2O} are the densities of the polymer blend and water, respectively [45].

$$\epsilon_b = \frac{(w_{wet} - w_{dry}) / \rho_{H_2O}}{(w_{wet} - w_{dry}) / \rho_{H_2O} + w_{dry} / \rho_p} \quad (1)$$

2.4.3. Pure water permeability (PWP) of substrates

For measuring PWP of the substrates, a lab scale RO setup was used

(Fig. 2). Feed pure water was run into the HF lumen side of the module.

Pure water permeation test was performed at the feed flow rate of 200 ml/min and transmembrane pressure of 1 bar for 1 h. Then, PWP was calculated as follows:

$$PWP = \frac{\Delta V}{A_m \Delta P \Delta t} \quad (2)$$

Where ΔV (mL) is the permeate volume (L) collected in an interval Δt (h), ΔP (bar) is the transmembrane pressure drop, and A_m (m²) is effective the external area of the membranes [45].

2.4.4. Surface porosity and pore size of the membrane (gas permeation test)

The mean pore size ($r_{p,m}$) and the effective surface porosity (ϵ/l_p) are the two important characteristics of the surface of the substrate [46]. The properties of the substrate skin layer can influence the active layer properties and performance [47]. These two parameters were evaluated by a constant pressure gas permeation test (Fig. 3). In the test, three fibers with a length of 5 cm were chosen to be installed in the gas permeation setup and one end of the HFs was closed with epoxy glue. Then, each hollow fiber was glued with epoxy into a fitting connected to a gas cylinder, from which nitrogen was fed into the lumen side. Nitrogen pressure was increased gradually from 1 bar to 5.5 bar and gas permeation flow rate was detected by a simple bubble flow meter versus various pressures.

The gas permeance is obtained by Eq. (3):

$$J^{exp} = \frac{\Delta V^{gas} * 101325}{R T A_m \Delta t \Delta P} \quad (3)$$

Where J^{exp} (mol m⁻²Pa⁻¹s⁻¹) is the permeance, ΔV is the volume of the bubble flow meter (m³), Δt is time (s) required for the bubble to pass through the flow meter, and ΔP (Pa) is the pressure difference. T is the absolute temperature (K), and R is the gas constant (J/mol.k). Here, A_m is the external membrane surface area (m²).

There are several models for calculating $r_{p,m}$ and ϵ/l_p of the porous membranes. In this paper, the conventional gas permeation test (GPT) model [48], as well as the new model of Hashemifard et al. [49], were used to obtain the above parameters. Using the conventional GPT model, $r_{p,m}$ and ϵ/l_p are obtained by the following equations [46].

$$J^{pred} = J_p + J_k \quad (4)$$

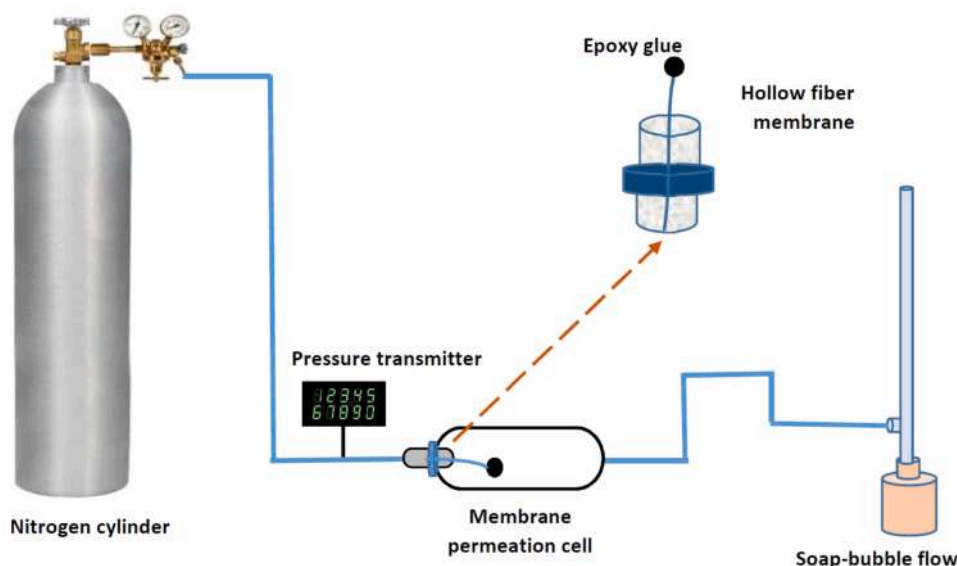


Fig. 3. Gas permeation testing setup.

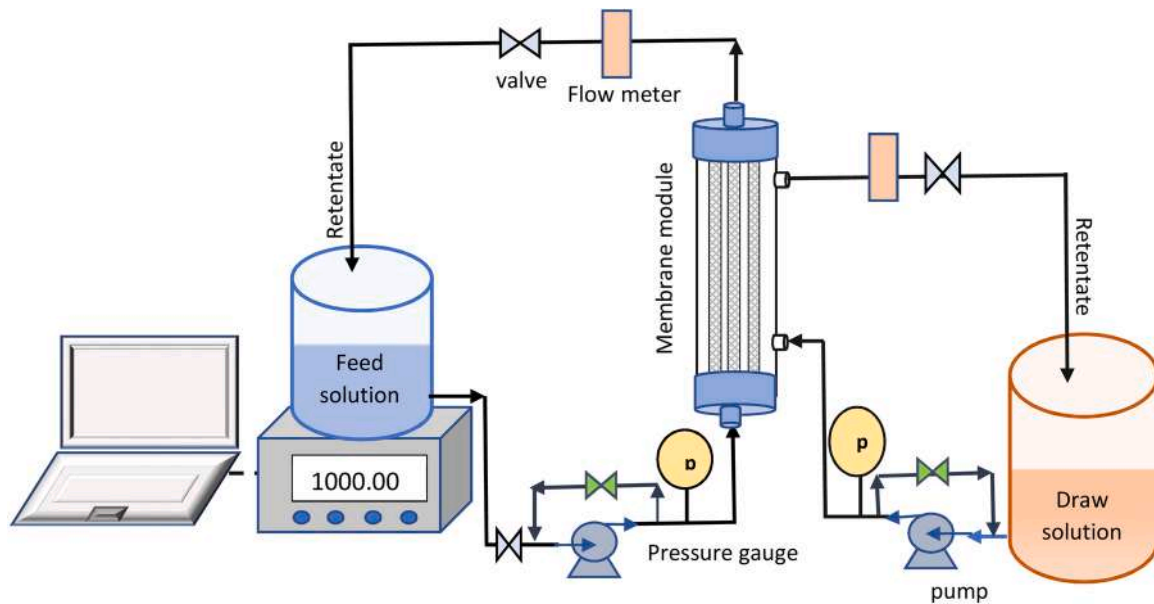


Fig. 4. Forward osmosis experimental setup (FO mode).

$$J_p = \left(\frac{2}{3}\right) \left(\frac{8RT}{\pi M}\right)^{0.5} \frac{r_{p,m} \varepsilon}{RT L_p} p \quad (5)$$

$$J_k = \frac{1}{8\mu} \frac{r_{p,m}^2 \varepsilon}{RT L_p} p \quad (6)$$

Hence, Eq. (4) can be written as,

$$J^{pred} = \alpha + \lambda p \quad (7)$$

Where J^{pred} , ($\text{mol m}^{-2}\text{Pa}^{-1}\text{s}^{-1}$) is the total gas permeance calculated for a given set of data including, $r_{p,m}$ (m), the effective pore length, L_p (m), the viscosity of the gas, μ (Pa s), is surface porosity, ε (-), the gas molecular weight, M (kg mol^{-1}), and the mean gas pressure in HF, p (Pa) [46]. J_k and J_p ($\text{mol m}^{-2}\text{Pa}^{-1}\text{s}^{-1}$) are Knudsen and Poiseuille flow fraction of the total permeance, respectively. Based on the above equations, $r_{p,m}$ and ε/L_p are obtained by the following equations, where α and λ are the intercept with y-axis and the slope of straight regression line drawn through the experimental permeance versus mean pressure plot.

$$r_{p,m} = \left(\frac{16}{3}\right) \left(\frac{\lambda}{\alpha}\right) \left(\frac{8RT}{\pi M}\right)^{0.5} \mu \quad (8)$$

$$\frac{\varepsilon}{L_p} = \frac{8\mu RT \lambda}{r_{p,m}^2} \quad (9)$$

Recently, a novel model was introduced by Hashemifard et al. [50] to find the surface porosity (ε) and surface pore size ($r_{p,m}$). The primary purpose of the model is to estimate the surface porosity (ε) and the pore length L_p separately [49]. The equations are as follows [50].

$$W = \alpha W_o + (1 - \alpha) W_{lt} \quad (10)$$

where, W_o and W_{lt} are the reduced flow rates in the orifice and the long tube, respectively. The orifice-long tube weight factor α , is obtained from the following equation:

$$\alpha = \frac{1}{1 + \frac{3}{4} \omega \left(1 + \frac{1}{3 + \frac{4}{9} \omega}\right) f(\delta)} \quad (11)$$

In Eq. (11) ω is the ratio of pore length to diameter. $f(\delta)$ is a function

of the rarefaction parameter δ .

$$\delta = \frac{\sqrt{\pi}}{2Kn} \quad (12)$$

In the above relation, Kn is the Knudsen number. The total permeance predicted is obtained from Eq. (13).

$$J^{pred} = \frac{Wn\sqrt{\pi}r_p^2 P_0}{v_m \Delta P M A_m} \quad (13)$$

In the above equation v_m is the gas most probable velocity, P_0 is upstream pressure and n is the number of the surface pores with $r_{p,m}$. According to the mentioned equations and using an iteration algorithm, $r_{p,m}$ and ε are obtained separately [49].

2.4.5. Determination of intrinsic separation properties of TFC-FO membrane

The water permeability (A) and salt permeability (B) coefficients of the TFC membranes were characterized using the experimental setup shown in Fig. 2 (RO setup). In the RO experiment, the feed was fed at 1 bar to the lumen side of HF, where the inner selective layer of HF faces the feed.

The water permeability (A) was calculated by Eq. (14) from the water permeation flux (J_w) obtained experimentally.

$$A = \frac{J_w}{\Delta P} \quad (14)$$

To obtain the salt retention ($R\%$) the following equation was used. It is noted that a 1000 ppm NaCl solution was applied as a feed solution to calculate $R\%$.

$$R\% = \left(1 - \frac{C_p}{C_f}\right) \times 100 \quad (15)$$

Where (C_p) and (C_f) are permeate and feed solution concentrations, respectively. Also, to measure the salt concentrations, a conductivity meter (WTW, inolab® Multi 9620 IDS) was employed. Finally, to determine the salt permeability (B), material balance based on the solution-diffusion theory was used:

$$B = A \left(\frac{100}{R\%} - 1\right) (\Delta P - \Delta \pi) \quad (16)$$

That P (bar) and π (bar) are hydraulic and osmotic pressure,

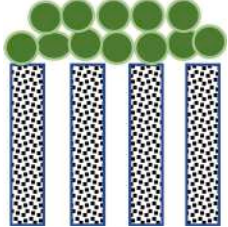

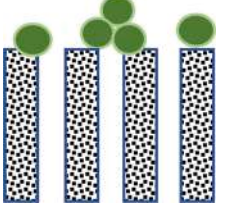
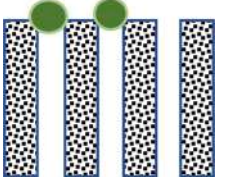
Table 2
Four fouling mechanisms based on Hermia's models [57].

Fouling mode	Flux expression
Cake formation	$J_v = \frac{J_{v0}}{(2K_{cf}J_{v0}^2t + 1)^{1/2}}$ $K_{cf} = kA^2$
Standard	$J_v = \frac{4J_{v0}}{(K_{pc}J_{v0}^{1/2}t + 2)^2}$ $K_{pc} = kA^{1/2}$
Intermediate blocking	$J_v = \frac{J_{v0}}{K_{ib}J_{v0}t + 1}$ $K_{ib} = kA$
Complete blocking	$J_v = J_{v0} \exp(-K_{cb}t)$ $K_{cb} = k$

Table 3
Five fouling mechanisms based on combined fouling models [58].

Fouling mode	Flux expression
Cake-complete	$V = \frac{J_{v0}}{K_b} (1 - \exp(\frac{-K_b}{K_c J_{v0}^2} (\sqrt{1 + 2K_c J_{v0}^2 t} - 1)))$
Cake-intermediate	$V = \frac{1}{K_i} \ln(1 + \frac{-K_i}{K_c J_{v0}} ((1 + 2K_c J_{v0}^2 t)^{1/2} - 1))$
Complete-standard	$V = \frac{J_{v0}}{K_b} (1 - \exp(\frac{-2K_b t}{2 + K_c J_{v0} t}))$
Intermediate-standard	$V = \frac{1}{K_i} \ln(1 + \frac{2K_i J_{v0} t}{2 + K_c J_{v0} t})$
Cake-standard	$V = \frac{2}{K_s} (\beta \cos(\frac{2\pi}{3} - \frac{1}{3} \arccos(\alpha)) + \frac{1}{3})$ $\alpha = \frac{8}{27\beta^3} + \frac{4K_s}{3K_c \beta^3 J_{v0}} - \frac{4K_s^2 t}{3K_c \beta^3}$ $\alpha = \sqrt{\frac{4}{9} + \frac{4K_s}{3K_c J_{v0}} - \frac{2K_s^2 t}{3K_c}}$

Table 4
Schematic of different fouling mechanisms.

Fouling mode	Schematic Diagram	Reversibility
Cake formation		Reversible
Standard		Irreversible
Intermediate blocking		Reversible- Irreversible
Complete blocking		Irreversible

respectively [45].

2.4.6. Evaluation of the FO performance of TFC membrane

The FO experiment was conducted using a lab scale FO setup shown in Fig. 4. DI water was circulated on the lumen side of HF as feed, while a 1 M NaCl solution was circulated as the draw solution (DS) on the shell side of the HF. Therefore, the process was in the FO mode, unless otherwise mentioned. The flow rates were 0.1 l/min and 0.2 l/min at the lumen and the shell side, respectively.

Water flux usually reached stability after 30 min. To track the weight variation of the feed solution Δm during the operation period Δt (1 h), an accurate digital balance was placed under the feed reservoir. The FO water flux (J_v) was calculated by the following equation [51]:

$$J_v = \frac{\Delta m}{\Delta t A_m} \quad (17)$$

That A_m is the internal surface area for both FO and PRO modes. Reverse salt flux was estimated by variation of salt concentration after operation time period, using Eq. (18) [52,53]. The reverse salt flux (J_s) was estimated from the change of salt concentration in the feed by Eq. (18) [52,53].

$$J_s = \frac{V_i C_i - V_0 C_0}{\Delta t A_m} \quad (18)$$

Where V_0 and V_t (l) are the initial and final volumes of the feed solution, respectively. C_0 and C_t (g/l) are the initial and final values of salt concentrations of the feed respectively during the operation time [52,53]. It should be noted that specific reverse solute flux (SRSF= J_s/J_v) is related to the intrinsic properties of the membrane according to Equation 19:

$$SRSF = J_s / J_v = \frac{B}{AnRT} \quad (13)$$

Here, n shows the number of ionic species formed during dissociation of the electrolyte solute [52,53]. Eq. (20) shows the water flux in the FO orientation by considering internal and external concentration polarization [54].

$$J_v = K \ln \left(\frac{A\pi_{draw} + B}{A\pi_{feed} + B + J_v \exp(-J_v/k)} \right) \quad (20)$$

Where π_{feed} (bar) and π_{draw} (bar) are the osmotic pressures of the feed and the draw solution, respectively, and J_v (L/m² h) is the FO water flux in FO mode K is the overall mass transfer coefficient obtained from Eq. (20), k is the mass transfer coefficient in the stream of feed [54].

$$\frac{1}{K} = \frac{1}{k_{lumen}} + \frac{d_i}{k_m d_{lm}} + \frac{d_i}{k_{shell} d_o} \quad (21)$$

Eq. (21) is derived due to the equality of mass transfer rate in different parts of the system i.e., lumen, shell and membrane and the concept of the series resistance of the mass transfer. Due to the presence of the active layer in the membrane lumen as the mass transfer surface, the inner surface of the membrane was considered for flux calculation. In this equation, k_m , k_{lumen} and k_{shell} (m/s) are the mass transfer coefficients of the membrane (in the pores of the substrate HF), the feed boundary layer (inner surface of the membrane), and the boundary layer of the draw solution (outer surface of the membrane), respectively. In Eq. (21) d_i , d_o and d_{lm} are the inner, outer and log mean diameters of the membranes, respectively.

The mass transfer coefficient related to the boundary layer of the feed and the draw solution can be calculated from the Sherwood number according to Eq. (22) [54].

$$Sh = \frac{k d_h}{D} \quad (22)$$

k (m/s) is the mass transfer coefficient and d_h (m) is the hydraulic diameter depending on the system geometry. Given that Eq. (20) is for

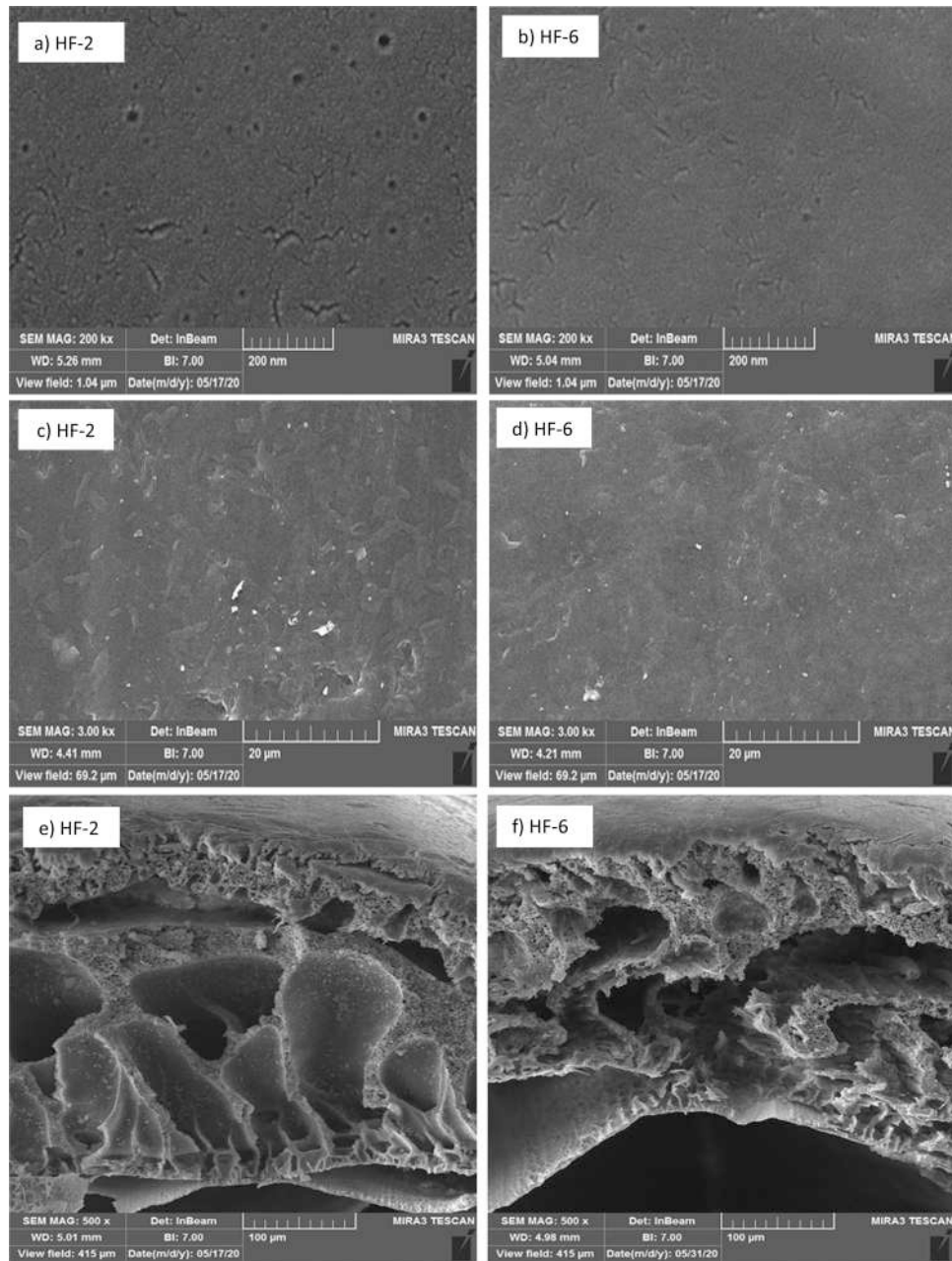


Fig. 5. SEM image of the two HF prepared substrates a,b inner surface of c,d outer surface e,f cross section.

the FO orientation and pure water flows through the lumen side, hence the boundary layer resistance can be almost neglected. Therefore, to calculate k_m , the overall mass transfer coefficient K is first obtained from the experimental J_v by Eq. (20), then calculate k_{shell} by Eq. (22), and subtract k_{shell} from K .

Eqs. (23) to (26) can be used to calculate the Sherwood number of the shell side depending on the length development of concentration and velocity profile. In regime I, both concentration and velocity profiles are being developed. In regime II, the velocity profile is fully developed while the concentration profile is still being developed. In regime III, concentration and velocity profiles are fully developed [55].

$$Sh_l = \left(\frac{2}{1 + 22Sc} \right)^{1/6} \left(\frac{ReScd_h}{L_m} \right)^{1/2} \quad (23)$$

$$d_h = \frac{4 * (\text{total flow area})}{(\text{total wetted perimeter})} = \frac{4(D_{module}^2 - Nd_o^2)}{\pi(d_{module} + Nd_o)} \quad (24)$$

Where N is the number of the HFs in the module, and D_{module} is the inner diameter of the HF module (m) [55].

$$Sh_{II} = 1.615[1 + 0.14(1 - \epsilon)^{-0.25}] \left(\frac{ReScd_h}{L_m} \right)^{1/3} \quad (25)$$

$$Sh_{III} = 3.66 + 1.2(\sqrt{1 - \phi})^{-0.8} \quad (26)$$

where L_m is the effective membrane length, d_h is the hydraulic diameter (m) and ϕ is hollow fiber packing density, which is obtained from the Eq. (27) [55].

$$\phi = 1 - N \left(\frac{d_o}{D_{module}} \right)^2 \quad (27)$$

the dimensionless Re and Sc are defined as,

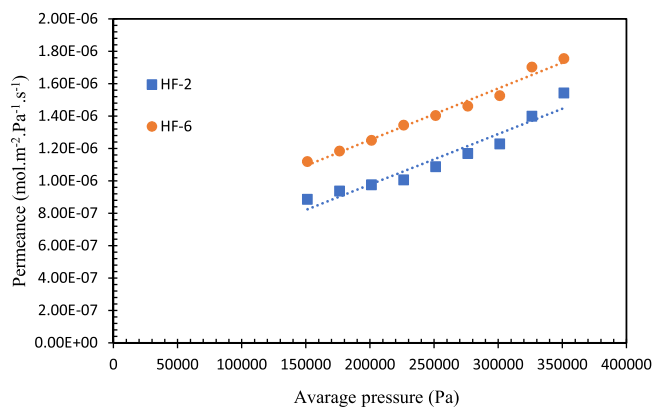


Fig. 6. The nitrogen permeance versus average pressure for the prepared HF substrates.

Table 5

Gas permeability test results applying two different models.

Model used	Sample	$r_{p,m}$ (nm)	ϵ (%)	L_p (μm)	ϵ/L_p (1/ m)
Conventional GPT model [48]	HF-2	336	–	–	9
	HF-6	224	–	–	21
Hashemifard et al. model [49]	HF-2	150	0.47	311	15.1
	HF-6	133	0.48	199	24.1

Table 6

Intrinsic separation properties of HF substrates.

properties	HF-2	HF-6
Outer diameter (mm)	1.16	1.12
Inner diameter (mm)	0.62	0.6
Overall porosity(ϵ_0)	77	73
PWP(LMH)	33	37

$$Re = \frac{\rho u d_h}{\mu} \quad (28)$$

and

$$Sc = \frac{\nu}{D} \quad (29)$$

μ (kg /m.s) is the fluid viscosity, ν is the fluid kinematic viscosity (m^2/s), u is the fluid velocity (m/s) and D (m^2/s) is the salt diffusion coefficient [54]. When fluid enters a hollow fiber membrane, the boundary layer begins to form adjacent to the fiber wall. As the fluid moves away from the inlet, the thickness of the boundary layer increases to the point where the boundary layer is completed, hence the flow is considered fully developed [56]. The length of developed concentration, L_{CR} , and that of velocity, L_{HR} , are obtained by Eqs. (30) and (31), respectively:

$$\frac{L_{CR}}{d_h} = 0.02 Re Sc^{0.66} (1 - \phi)^{0.25} \quad (30)$$

$$\frac{L_{HR}}{d_h} = 0.02 Re (1 - \phi)^{0.25} \quad (31)$$

If both concentration and velocity profiles are being developed but the effects of the length of velocity development need to be considered, the average Sherwood number, calculated by Eq. (25), is used [55].

$$Sh = (Sh_I^3 + Sh_{II}^3)^{1/3} \quad (32)$$

Similarly, if the velocity profile is fully developed but the concentration profile is not developed, the following equation can be used to

obtain the average Sherwood number:

$$Sh = (Sh_I^3 + Sh_{II}^3)^{1/3} \quad (33)$$

As mentioned earlier, the membrane mass transfer coefficient, k_m , is calculated by subtracting k_{shell} , obtained by the dimensionless analysis, from K . Then, the structural parameter S (m) is calculated by Eq. (34) [45].

$$S = \frac{D}{k_m} \quad (34)$$

2.4.7. FO fouling experiments of TFC-FO membrane

The fouling mitigation potential of the newly developed TFC membranes was studied by dissolving sodium alginate in FO feed. Before performing the fouling tests, the baseline tests were conducted with feed DI water and the DS containing 1 M NaCl to determine J_{v0} as the baseline water flux. Then, the sodium alginate solution (200 mg/L) was added to the feed stream while NaCl concentration in DS was kept 1 M, and 4 h FO experiment was conducted.

Then the fouling mechanism of the fabricated membranes was determined based on the simple and combined models of Hermia. In general, depending on the size and shape of the foulant molecules, the characteristics of the membrane surface, as well as the pore size distribution of the membrane.

The fouling mechanism was examined by the Hermia model. Depending on the size and shape of the foulant molecules, the characteristics of the membrane topology, and distribution of the pore size of the membrane, the fouling mechanisms are classified into the following four types: 1- Cake formation 2- Standard 3- Intermediate blocking 4- Complete blocking. Table 2 shows the mechanisms along with their flux equations [57]. In addition, five extra fouling models are considered to investigate the simultaneous effects of each of the four mechanisms (Table 3). Each one possesses two parameters. With the help of Solver plugin in Excel software and minimizing the error between the laboratory data and the flux estimated by the models, the best fouling mechanism was selected. J_v : Water Flux K_{cf} : Cake formation parameters K_{pc} : standard fouling parameter K_{ib} : intermediate blocking parameter K_{cb} : complete blocking parameter k : constant kinetics parameter

V is the volume filtered and K_b , K_c , K_i , K_s are the models parameters.

Table 4 shows schematics of the different mechanisms of membrane fouling for comparison.

After performing the fouling test with a feed containing sodium alginate, the membrane lumen was rinsed with DI water for 30 min at a flow rate three times that of the feed. Then pure water flux was measured via forward osmosis system with pure water feed to calculate the percentage of water flux recovery ratio (FRR) [23]:

$$FRR(\%) = \frac{J_{v1}}{J_{v0}} \times 100 \quad (35)$$

Membrane resistance (R_m) (cm^{-1}), total resistance (R_t) (cm^{-1}), irreversible resistance (J) (cm^{-1}) and reversible resistance (R_r) (cm^{-1}) can also be derived from the following equations [59]:

$$R_m = \frac{\Delta\pi}{\mu J_{v0}} \quad (36)$$

$$\left(R_t = \frac{\Delta\pi}{\mu J_{v2}} \right) \quad (37)$$

$$R_{ir} = \frac{\Delta\pi}{\mu J_{v1}} - R_m \quad (38)$$

$$R_r = 100 - R_m - R_{ir} \quad (39)$$

In the above equations, J_{v2} ($\text{L}/\text{m}^2\text{h}$) is the flux in the presence of sodium alginate in the feed, which is the same as J , reported in Table 2. $\Delta\pi$ is the osmotic pressure (Pa), and μ is the viscosity (Pa.h) of water.

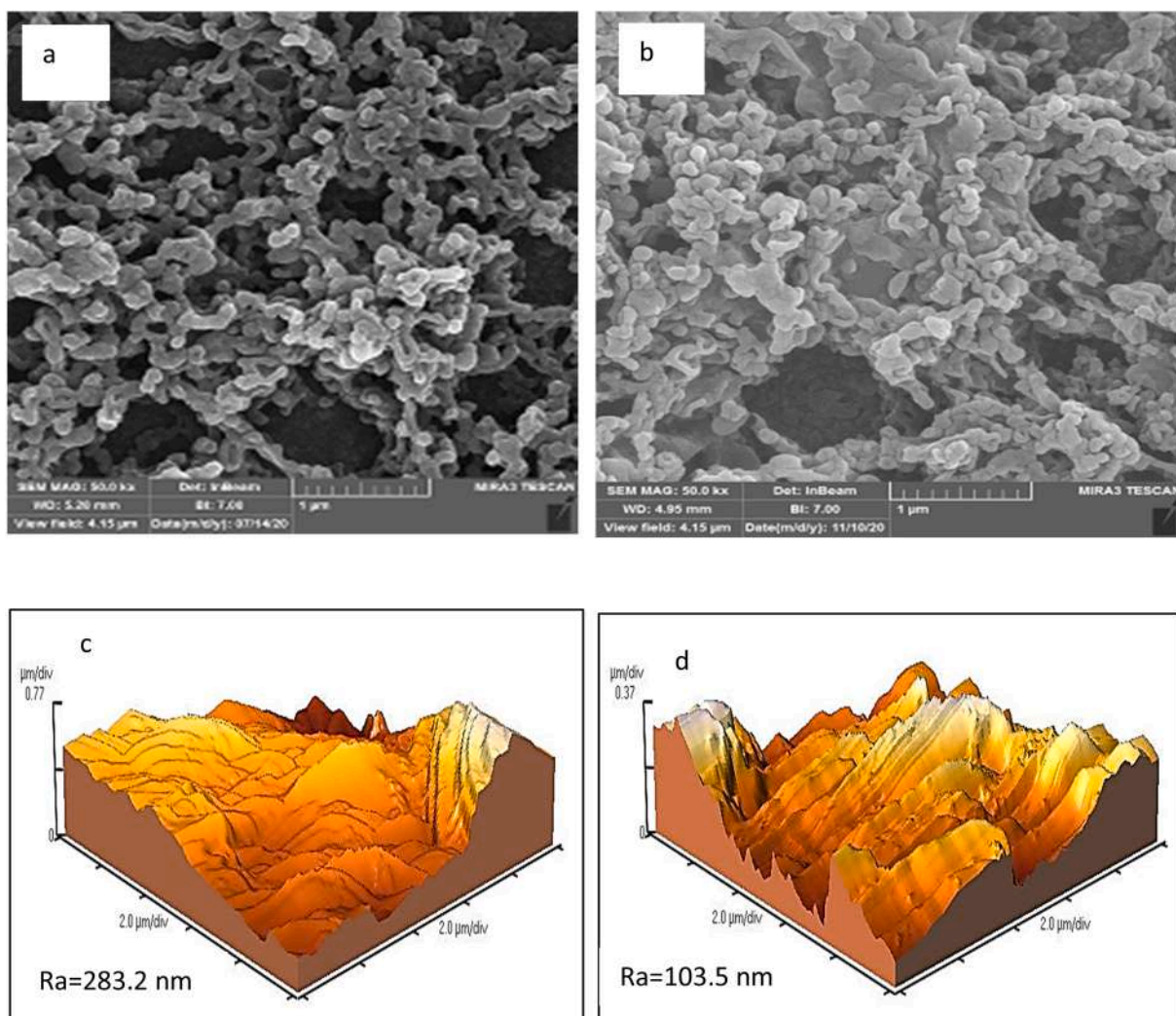


Fig. 7. FESEM image of the two TFC membranes a) TFC-2, b) TFC-6 and AFM image of the two TFC membranes c) TFC-2, d) TFC-6.

Table 7

Intrinsic separation properties of TFC hollow fiber membranes.

TFC membrane	A (LMHbar ⁻¹)	B (LMH)	B/A (bar)	L _{CR} (m)	L _{HR} (m)	k _{shell} (m/s)	k _m (m/s)	S* (m)
TFC-2	3.78 ± 0.02	2.09 ± 0.03	0.55	1.44	0.019	4.77 × 10 ⁻⁶	2.30 × 10 ⁻⁷	0.0069
TFC-6	1.47 ± 0.05	0.39 ± 0.01	0.26	1.44	0.019	4.77 × 10 ⁻⁶	7.79 × 10 ⁻⁷	0.0020

* FO mode, module length equal to 0.1 m.

3. Result and discussion

3.1. Effect of air gap on the properties of substrates

Fig. 5 shows SEM images of the inner and outer surfaces and the cross section of the substrates HF-2 and HF-6. From the figure, the morphology of the inner surfaces (Figs. 5a and 5b) and the outer surfaces (5c and 5d) are both relatively dense and almost smooth. The surface is expected to become denser as the air gap distance becomes longer, which can be observed more clearly in the inner surface by comparing Figs. 5a and 5b. As for the cross-section, comparing Figs. 5e and 5f, HF-2 has a larger number of finger-like pores, while the HF-6 membrane exhibits a larger fraction of sponge-like structure, again confirming the trend of the denser HF formation with an increase in the air gap distance.

The above trend is reflected in the results of gas permeation test.

Fig. 6 shows the permeance versus system average pressure for evaluating the effective surface porosity and mean pore size of the two

substrates. Permeance increased almost linearly with increasing average pressure for both substrates. Using the slope (λ) and intercept (α) of the fitted straight lines, r_{pm} and ϵ/L_p were calculated by the conventional GPT model. The model developed by Hashemifard et al. allowed the evaluation of r_{pm} , ϵ , and L_p . The results so obtained are summarized in Table 5.

Increasing the air gap increased the molecular orientation of the polymer in the nascent HF by gravity before it entered the coagulation bath, decreasing the mean pore size of the substrate surface considerably [23,60]. According to Hashemifard et al.'s model, The difference in surface porosity (ϵ) of the two HFs membranes is only a fraction of 1%.

The results from Hashemifard et al. model confirms the results of the conventional GPT model. According to the Hashemifard et al. model the effective length decreases (L_p) faster than the surface porosity (ϵ) increase from HF-2 to HF-6. Therefore, the effective surface porosity (ϵ/L_p) increases. The decrease in L_p is caused by the stronger stress applied to the fibers during gelation after traveling a longer air gap distance [61].

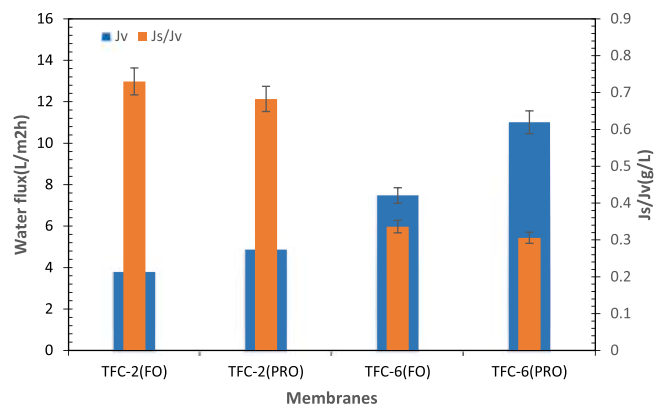


Fig. 8. FO water flux and specific reverse salt flux of HF-2 and HF-6 membrane in FO and PRO model (feed solution: DI water, draws solution: 1 M NaCl solution).

Table 6 summarizes the bulk properties of the HF such and the HF dimensions, over all porosity and PWP.

In Table 6, PWP of HF-6 is higher than HF-2 despite the larger surface pore size of H-2. It is due to the higher effective surface porosity of the HF-6. HF-2 membrane has higher overall porosity and larger inner and outer diameter than HF-6 membrane. Again, this is because of the stronger stress applied to the fibers during the solvent exchange step in the coagulation bath [61]. In fact, the effects of air gap on the properties of the substrate are very complex. Although there are a number of researches on these effects, conflicting observations have been reported [61], probably due to differences in the type of polymer, the formulation of the polymer solution, as well as differences in the conditions of the membrane synthesis.

3.2. Effect of air gap on the properties of TFC membranes

Fig. 7a and b illustrate the surface FESEM image of TFC-2 and TFC-6 membranes, respectively. The smooth surfaces of the substrates are now covered with the selective layer with ridge and valley morphology. There is no significant difference between the two images, even though the surface of TFC-6 is expected to be smoother because of the smaller surface pore size of the substrate HF-6. Fig. 7c and d exhibit the 3D AFM images of the surface of the synthesized membranes along with average surface roughness (Ra). The average surface roughness of the membranes confirms the smoother surface of the TFC-6 membrane.

Table 7 shows the intrinsic separation properties of the membrane including the water permeability (A) and salt permeability (B) coefficients and intrinsic selectivity (B/A) as well as the developed length of concentration (L_{CR}) and velocity profile (L_{HR}), k_{shell} , k_m and the structural parameter of the membrane (S). A, B and B/A are larger for TFC-2 membrane than for THF-6 membrane. This is because of the more defects at the active layer of THF-2 caused by the larger mean pore size

Table 8

FO performance of various membranes used for FO process in FO and PRO mode.

Sample	performance				Experimental condition		Reference
	AL-FS (FO)		AL-DS (PRO)		Feed solution	Draw solution	
	J_v (LMH)	J_s/J_v (g/L)	J_v (LMH)	J_s/J_v (g/L)			
PVC/PC PA HF(TFC-6)	7.48	0.33	11	0.3	DI water	1 M NaCl	Present work
PBINF HF			3.48	–	DI water	2 M NaCl	[63]
Matrimid PA HF	11.8	0.21	50.5	0.07	DI water	2 M NaCl	[27]
Toyobo HF	8	0.07	15	N/A	DI water	1 M NaCl	[64]
PAN PA HF	24.71	0.77	36.57	0.512	DI water	1 M NaCl	[36]
Samsung Cheil HF	10	0.36	19	0.47	DI water	1 M NaCl	[65]
Aquaporin A/S HF	13.2	0.14	21	0.18	DI water	1 M NaCl	[66]
PVDF PA HF	10.6	0.23	12.2	3.21	DI water	1 M NaCl	[67]

of HF-2. The value of B/A is of great importance as the membrane intrinsic selectivity. This value was 0.39 for HF-6, which is quite acceptable compared to other reports in the field of FO hollow fiber membranes, e.g. Lu et al. [27], Ren et al. [36] and Lim et al. [23] reported B/A = 0.38, 0.75 and 0.12, respectively. By comparing the length of the fully developed velocity and concentration.

profile (LCR and LHR) reported in Table 7, it is clear that the velocity distribution has developed.

while the concentration distribution has not yet developed. Therefore, it is known that Eq.

(33) should be used to calculate Sherwood number, and then k_{shell} by Eq. (22).

The k_{shell} values obtained for TFC-2 and TFC-6 are very close to each other, which is natural since the geometrical and hydrodynamic conditions are almost identical for both TFC-2 and TFC-6 modules. The only difference is the HF outer diameter. Comparing k_m of TFC-2 and TFC-6, TFC-6's k_m is higher than that of TFC-2. There are two factors that may affect k_m . One is the effective surface porosity of the substrate and the other the overall surface porosity. When these factors increase k_m will increase. While the effective surface porosity of substrate HF-6 is higher than HF-2 (Table 5), the overall porosity of HF-6 is lower than HF-2 (Table 6). Therefore, one can conclude that the effect of surface porosity is more dominant than the overall porosity [43]. Also, due to the smaller structural parameter, TFC-6 will perform better in FO than TFC-2.

3.3. Air gap effect on the performance of TFC membranes

The water flux (J_v) and SRSF (J_s/J_v) of the two fabricated TFC membranes are shown in Fig. 8. The experiments were performed using DI water as feed and 1 M NaCl aqueous solution as draw solution (DS), under FO and PRO modes. Fig. 8 shows that water flux of PRO mode is higher than FO mode, due to the lower ICP in the former mode [7]. SRSF is an important parameter that indicates selectivity of the membrane in FO systems [62]. According to Equation (19), SRSF is a function of the intrinsic properties of the membrane and is independent of the mode of membrane [18], that is almost confirmed by Fig. 8. Comparing TFC-2 and TFC-6, TFC-6's J_s/J_v is lower than that of TFC-2, meaning selectivity of TFC-6 is higher. This is because TFC-6 has less defects, due to the smaller surface pore size and higher surface porosity of substrate (Table 3). Thus, TFC-6 is expected to exhibit better FO performance than TFC-2.

Also, Table 8 lists FO performance of various membranes used for FO process in FO and PRO mode. The performance of the membrane (TFC-6) fabricated in this work is acceptable in comparison with the membranes given in the table. A few of the membranes shown in the table are commercial membranes.

3.4. Fouling and cleaning of TFC HF membranes under FO operation

Fouling test was performed for the two TFC HFs for a time period of

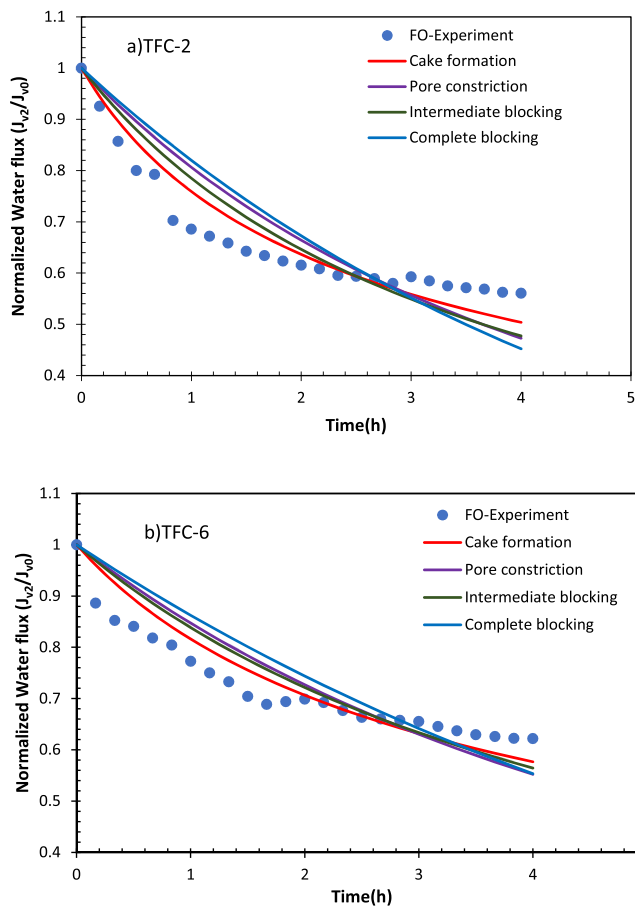


Fig. 9. Fouling tendency of the fabricated TFC hollow fiber membranes (experimental data and Hermia fouling model).

4 h. Fig. 9 shows the changes in the normalized flux over time for the two fabricated membranes due to fouling. It shows that the fouling of TFC-2 is more severe. Further reduction of flux for membrane TFC-2 was due to the formation of a defective selective layer and therefore decreased the osmotic driving force. One of the reasons for the severe fouling is that the selective layer is on the lumen side and the foulant containing feed is also supplied to the lumen side. Some research results showed that the fouling becomes less severe when the dense layer is fabricated on the outer surface and the feed flows in the shell side [23]. However, when the feed does not contain suspended solids, as in the current work, and the chance of feed channel lockage is less, the selective layer on the lumen side is not necessarily a poor choice since the turbulence in the feed stream is enhanced in the lumen of HFs. Fig. 9 shows the model fitted lines, and Fig. 10 shows the experimental V_t , the amount of permeate collected, versus t , both experimental and model fitted. The reason that the data trend is close to the straight line is the short test time and low water flux.

The errors of the fitting data are listed for all the simple and combined Hermia models in Table 9. In Table 4, standard and complete fouling are irreversible or irremovable, while cake fouling is reversible [68]. Fitting the data with the simple Hermia models shows that, the cake model has the least error. On the other hand, the fitting with the combined Hermia models show that the Cake-complete and Cake-standard models have the least errors. The errors are similar for the latter two models since the severest state of the standard fouling is the complete fouling.

Therefore, it can be concluded that the primary cause for fouling is the reversible cake formation. The organic foulant, sodium alginate in this work, forms a gel-like layer on the HF. As FO is not a pressure-driven process, the gel-like layer is weakly bound to the HF surface and the

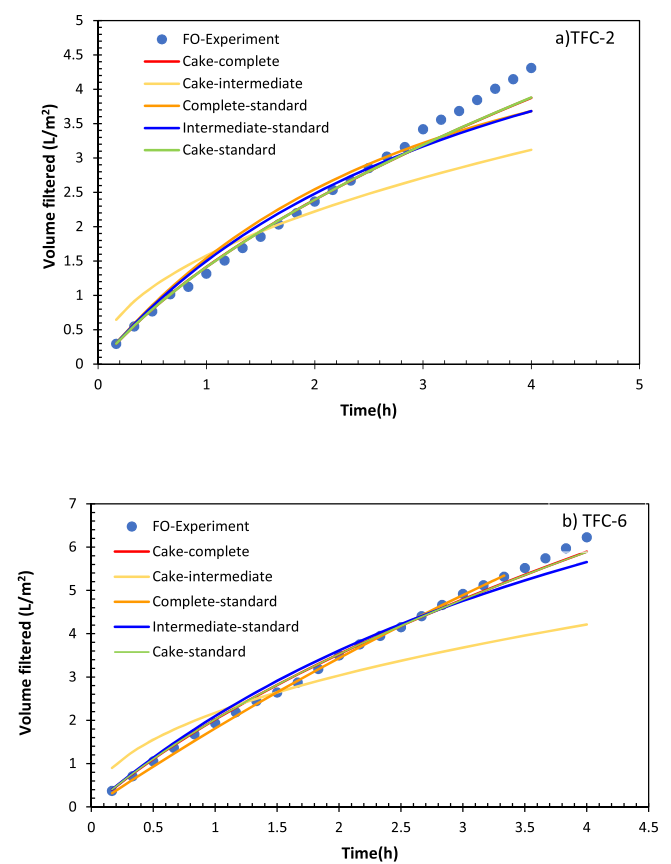


Fig. 10. Fouling tendency of the fabricated TFC hollow fiber membranes (experimental data and Combined fouling model).

Table 9

Model fit error for two fabricated Hollow fiber membranes.

Model	Model fit error for TFC-2 (model constant)	Model fit error for TFC-6 (model constant)
Cake formation	5.52 ($K_{cf}:0.09 \text{ hm}^4/\text{L}^2$)	4.33 ($K_{cf}:0.06 \text{ hm}^4/\text{L}^2$)
Standard	9.25 ($K_{pc}:0.16 \text{ m}^2/\text{L}^{1/2}\text{h}^{1/2}$)	6.69 ($K_{pc}:0.12 \text{ m}^2/\text{L}^{1/2}\text{h}^{1/2}$)
Intermediate blocking	7.90 ($K_{ib}:0.14 \text{ m}^2/\text{L}$)	5.85 ($K_{ib}:0.1 \text{ m}^2/\text{L}$)
Complete blocking	10.70 ($K_{cb}:0.19 \text{ 1/h}$)	7.58 ($K_{cb}:0.14 \text{ 1/h}$)
Cake-complete	4.48 ($K_c:0.26 \text{ hm}^4/\text{L}^2$, $K_b:0.001 \text{ 1/h}$)	3.60 ($K_c:0.09 \text{ hm}^4/\text{L}^2$, $K_b:0.001 \text{ 1/h}$)
Cake-intermediate	23.82 ($K_c:8177.8 \text{ hm}^4/\text{L}^2$, $K_i:0.018 \text{ m}^2/\text{L}$)	27.54 ($K_c:2144.76 \text{ hm}^4/\text{L}^2$, $K_i:0.03 \text{ m}^2/\text{L}$)
Complete-standard	9.18 ($K_b:0.37 \text{ 1/h}$, $K_s:0.05 \text{ m}^2/\text{L}$)	6.12 ($K_b:0.1 \text{ 1/h}$, $K_s:0.11 \text{ m}^2/\text{L}$)
Intermediate-standard	7.87 ($K_i:0.001 \text{ m}^2/\text{L}$, $K_s:0.27 \text{ m}^2/\text{L}$)	6.06 ($K_i:0.0009 \text{ m}^2/\text{L}$, $K_s:0.15 \text{ m}^2/\text{L}$)
Cake-standard	4.41 ($K_c:0.24 \text{ hm}^4/\text{L}^2$, $K_s:0.03 \text{ m}^2/\text{L}$)	3.74 ($K_c:0.08 \text{ hm}^4/\text{L}^2$, $K_s:0.26 \text{ m}^2/\text{L}$)

fouling is largely reversible [69].

Fig. 11 shows the irreversible resistance (R_{ir}), reversible resistance (R_r), total resistance (R_t) and membrane resistance (R_m) for both TFC HFs. In Fig. 11, the fouling contains both reversible and irreversible components. The irreversible fouling is due to the complete or standard components of the combined Hermia model and the reversible fouling due to the Cake mechanism. The figure shows that R_r is more than R_{ir} , and particularly in TFC-6 membrane, R_{ir} is very low due to the more defect-free surface of its active layer. In addition, FRR was 96.5% and 87.94% for membrane TFC-6 and TFC-2, respectively.

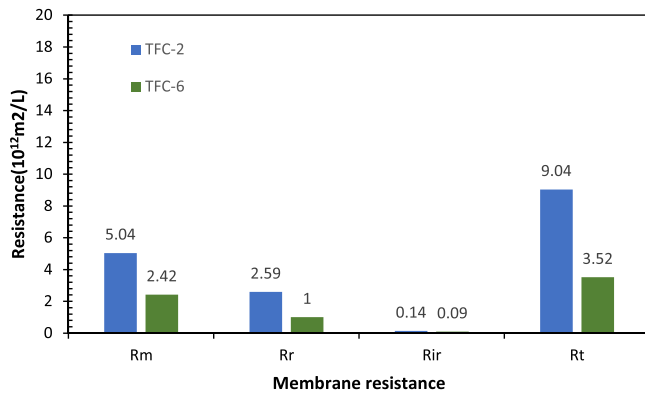


Fig 11. Fouling parameters of TFC-2 and TFC-6.

3.5. Effect of fiber length on the performance of TFC-FO membranes

Table 10 depicts the flux and different mass transfer coefficients obtained from the experiment and models for two different fiber lengths. Only TFC-6 is considered in this investigation. For better comparison of the modeling and laboratory results, Sherwood numbers were calculated according to regimes I, II and the combination of the two regimes. However, based on the developed concentration length, L_{CR} , and the developed velocity length, L_{HR} , shown in Table 7, the regime II seems the most appropriate.

In Table 10, in the experimental section, we obtained the water flux through the experiment and K was obtained according to Eq. (20). Then k_m in Table 7 was used to calculate k_{shell} and the Sherwood number by Eqs. (21) and (22), respectively. In the model section, Sherwood number was calculated by Eqs. (23), (25) and (33) and k_{shell} was calculated by Eq. (22). K was then obtained by Eq. (21) using k_m listed in Table 7. Finally, the water flux was calculated by Eq. (20).

In Table 10, the experimental water flux decreased considerably with the increasing module length, while according to the model, the water flux change with the module length is insignificant.

When k_{shell} and k_m , which affect water flux, are compared, k_m is much smaller than k_{shell} (see Table 7). In other words, mass transfer resistance is governed by k_m that remains constant for any fiber length. Therefore, based upon the model calculation, the fiber length does not have any significant effect on the membrane flux. Thus, the model does not accurately describe the module behavior.

There are some reports in the literature on the effect of HF length on the water flux. Zhong et al. [30] observed that the water flux decreased with increasing length of the membrane module. In another study, Ren et al. [70] used CFD software for different module lengths of 0.1, 0.5 and 1 m. They observed that when the module length increased, the boundary layer expanded more and was highly resistant against the mass transfer rate. Ren et al. [70] further suggested that it would be better to use long modules for low fluxes and to use short length modules for high fluxes due to the length effect. This means that for the low flux module, it is better to increase the module length, to increase the module productivity by the increase of membrane area, while it is more desirable to increase the number of HFs, keeping the module length constant, for the high flux module. However, the effect of module length is still a

controversial issue and more in-depth studies are required considering the membrane type, flow conditions, type of draw and feed solution, as well as membrane module diameter.

The experimental part of Table 10 also shows that the change in the membrane length does not influence the specific reverse salt flux significantly. The slight discrepancy is probably due to the experimental error.

4. Conclusion

In this research, forward osmosis hollow fiber membranes were successfully fabricated by spinning the substrate hollow fiber from a blend solution of polycarbonate and polyvinyl chloride and coating with an active polyamide layer onto the lumen surface. The membranes were characterized and their FO performance tested in terms of water flux, reverse salt flux and membrane fouling. In particular, FO performance was investigated at different air gap distances in the HF spinning and different fiber lengths in the FO module. The following conclusions are drawn from the results.

Air gap influences the characteristics of the substrate surface e.g., the effective porosity and mean pore size. In addition, air gap can affect the membrane dimensions, morphology and overall porosity. The surface characteristics of the substrate have a significant influence on the structure of the active layer and the performance of the TFC membrane in forward osmosis process as well as the fouling behavior of the membrane. The higher surface porosity of the substrate HF has favorable effects on the TFC HF in two ways; one that the surface of TFC HF becomes more defect free, suppressing the reverse salt transport and the other that enhancing mass transfer coefficient in the membrane, i.e., reducing the concentration polarization, which leads to higher water flux. Also, the mechanism of fouling was determined using the simple and combined Hermia models. The primary cause of fouling with sodium alginate is due to the reversible cake formation. There are also minor contributions of irreversible complete and standard fouling. The irreversible fouling is suppressed in the TFC HF fabricated from the substrate HF spun with longer air gap distance. Flux recovery was also better for the TFC HF with longer air gap distance. It is concluded that the membrane with smaller structural parameter due to higher air gap, will show higher performance. Also, increasing the air gap by creating a defect-free active layer showed a positive effect on the control of membrane fouling. According to the laboratory data, water flux decreased with the fiber length, contrary to the model simulation. This indicates that the model does not present well the effect of length and therefore the effects of the boundary layer on water flux. Due to the effect of membrane length on the flux, in the low flux mode to increase the membrane area and higher productivity, it is recommended to increase the membrane length. While in the high flux mode, to increase the membrane area, the number of fibers should be increased. The effect of fiber length is a controversial issue and more studies are needed.

CRedit authorship contribution statement

Z. Alihemati: Methodology, Experiments, Writing – original draft. S. A. Hashemifard: Conceptualization, Methodology, Writing – review & editing. T. Matsuura: Reviewing, Commenting and Editing. A. F.

Table 10

The effect of membrane length on water flux and specific reverse salt flux.

Module	Experimental				Model								
	J_v	k_{shell}	Sh_{shell}	Js/J_v	regime I			regime II			combined regime		
					Sh_{shell}	k_{shell}	J_v	Sh_{shell}	k_{shell}	J_v	Sh_{shell}	k_{shell}	J_v
TFC-6 (10 cm)	7.48	4.95×10^{-6}	27.07	0.33	26.12	4.77×10^{-6}	7.45	49.41	9.03×10^{-6}	7.72	51.73	9.41×10^{-6}	7.73
TFC-6 (19 cm)	3.63	0.28×10^{-6}	1.55	0.28	18.95	3.46×10^{-6}	7.24	39.89	7.29×10^{-6}	7.64	41.27	7.54×10^{-6}	7.66

$k_m = 7.79 \times 10^{-7}$ m/s, Re = 256.74. All of the fluxes and mass transfer coefficients have the same units in LMH and m/s, respectively.

Ismail: Writing – review & editing.

Declaration of Competing Interest

The authors declare that they have no known competing financial interests or personal relationships that could have appeared to influence the work reported in this paper.

Acknowledgments

This study was funded by the Iran National Science Foundation (INSF) with Grant number: 98011635. The authors gratefully acknowledge Persian Gulf University (PGU) and Universiti Teknologi Malaysia (UTM) for their financial support.

References

- [1] T.-S. Chung, et al., Emerging forward osmosis (FO) technologies and challenges ahead for clean water and clean energy applications, *Curr. Opin. Chem. Eng.* 1 (3) (2012) 246–257.
- [2] A.A. Shah, et al., Facile integration of halloysite nanotubes with bioadhesive as highly permeable interlayer in forward osmosis membranes, *J. Ind. Eng. Chem.* 73 (2019) 276–285.
- [3] G. Blandin, et al., Efficiently combining water reuse and desalination through forward osmosis—reverse osmosis (FO-RO) hybrids: a critical review, *Membranes* 6 (3) (2016) 37.
- [4] A. Behboudi, et al., Preparation and characterization of asymmetric hollow fiber polyvinyl chloride (PVC) membrane for forward osmosis application, *Sep. Purif. Technol.* 270 (2021), 118801.
- [5] S.N. Ellis, et al., Nitrogen rich CO₂-responsive polymers as forward osmosis draw solutes, *Ind. Eng. Chem. Res.* 58 (50) (2019) 22579–22586.
- [6] J.S. Yong, W.A. Phillip, M. Elimelech, Reverse permeation of weak electrolyte draw solutes in forward osmosis, *Ind. Eng. Chem. Res.* 51 (41) (2012) 13463–13472.
- [7] K.Y. Wang, R.C. Ong, T.-S. Chung, Double-skinned forward osmosis membranes for reducing internal concentration polarization within the porous sublayer, *Ind. Eng. Chem. Res.* 49 (10) (2010) 4824–4831.
- [8] X. Wu, et al., Microporous carbon from fullerene impregnated porous aromatic frameworks for improving the desalination performance of thin film composite forward osmosis membranes, *J. Mater. Chem. A* 6 (24) (2018) 11327–11336.
- [9] L. Upadhyaya, X. Qian, S.R. Wickramasinghe, Chemical modification of membrane surface—overview, *Curr. Opin. Chem. Eng.* 20 (2018) 13–18.
- [10] D.M. Reurink, et al., Polyelectrolyte Multilayers for Forward Osmosis, Combining the Right Multilayer and Draw Solution, *Ind. Eng. Chem. Res.* 60 (19) (2021) 7331–7341.
- [11] S. Benavides, A.S. Oloriz, W.A. Phillip, Forward osmosis processes in the limit of osmotic equilibrium, *Ind. Eng. Chem. Res.* 54 (1) (2015) 480–490.
- [12] S. Zhao, K. Huang, H. Lin, Impregnated membranes for water purification using forward osmosis, *Ind. Eng. Chem. Res.* 54 (49) (2015) 12354–12366.
- [13] A. Blazyte, et al., Effect of size fractionated alginate-based transparent copolymer particles on initial bacterial adhesion of forward osmosis membrane support layer, *J. Ind. Eng. Chem.* 94 (2021) 408–418.
- [14] M. Shibuya, et al., Novel CA/PVDF nanofiber supports strategically designed via coaxial electrospinning for high performance thin-film composite forward osmosis membranes for desalination, *Desalination* 445 (2018) 63–74.
- [15] R. Dai, et al., Porous metal organic framework CuBDC nanosheet incorporated thin-film nanocomposite membrane for high-performance forward osmosis, *J. Membr. Sci.* 573 (2019) 46–54.
- [16] X. Song, et al., Polyamide membrane with an ultrathin GO interlayer on macroporous substrate for minimizing internal concentration polarization in forward osmosis, *Chem. Eng. J.* 412 (2021), 128607.
- [17] X. Bao, et al., Fouling mechanism of forward osmosis membrane in domestic wastewater concentration: Role of substrate structures, *Chem. Eng. J.* 370 (2019) 262–273.
- [18] H.-E. Kwon, et al., High performance polyacrylonitrile-supported forward osmosis membranes prepared via aromatic solvent-based interfacial polymerization, *Sep. Purif. Technol.* 212 (2019) 449–457.
- [19] D.Y. Kim, et al., Polyvinyl alcohol hydrogel-supported forward osmosis membranes with high performance and excellent pH stability, *J. Ind. Eng. Chem.* 99 (2021) 246–255.
- [20] L. Xia, et al., Novel commercial aquaporin flat-sheet membrane for forward osmosis, *Ind. Eng. Chem. Res.* 56 (41) (2017) 11919–11925.
- [21] M.R. Chowdhury, L. Huang, J.R. McCutcheon, Thin film composite membranes for forward osmosis supported by commercial nanofiber nonwovens, *Ind. Eng. Chem. Res.* 56 (4) (2017) 1057–1063.
- [22] S.A. Hashemifard, et al., *Synthetic polymeric membranes for gas and vapor separations, in Synthetic Polymeric Membranes for Advanced Water Treatment, Gas Separation, and Energy. Sustainability*, Elsevier, 2020, pp. 217–272.
- [23] S. Lim, et al., Defect-free outer-selective hollow fiber thin-film composite membranes for forward osmosis applications, *J. Membr. Sci.* 586 (2019) 281–291.
- [24] Z. Alihemati, et al., Current status and challenges of fabricating thin film composite forward osmosis membrane: A comprehensive roadmap, *Desalination* 491 (2020), 114557.
- [25] M. Mohammadifakhr, et al., Single-step synthesis of a polyelectrolyte complex hollow-fiber membrane for forward osmosis, *Sep. Purif. Technol.* 264 (2021), 118430.
- [26] C.F. Wan, et al., Design and fabrication of hollow fiber membrane modules, *J. Membr. Sci.* 538 (2017) 96–107.
- [27] L. Luo, et al., Novel thin-film composite tri-bore hollow fiber membrane fabrication for forward osmosis, *J. Membr. Sci.* 461 (2014) 28–38.
- [28] S.-P. Sun, T.-S. Chung, Outer-selective pressure-retarded osmosis hollow fiber membranes from vacuum-assisted interfacial polymerization for osmotic power generation, *Environ. Sci. Technol.* 47 (22) (2013) 13167–13174.
- [29] R. Wang, et al., Characterization of novel forward osmosis hollow fiber membranes, *J. Membr. Sci.* 355 (1) (2010) 158–167.
- [30] P. Zhong, et al., Development of thin-film composite forward osmosis hollow fiber membranes using direct sulfonated polyphenylenesulfone (sPPSU) as membrane substrates, *Environ. Sci. Technol.* 47 (13) (2013) 7430–7436.
- [31] Z.-L. Qiu, et al., Cross-linked PVC/hyperbranched polyester composite hollow fiber membranes for dye removal, *React. Funct. Polym.* 122 (2018) 51–59.
- [32] Peng, N., et al., Evolution of polymeric hollow fibers as sustainable technologies: Past, present, and future. *Progress in Polymer Science*, 2012. 37(10): p. 1401–1424.
- [33] S. Chou, et al., Characteristics and potential applications of a novel forward osmosis hollow fiber membrane, *Desalination* 261 (3) (2010) 365–372.
- [34] L. Shi, et al., Effect of substrate structure on the performance of thin-film composite forward osmosis hollow fiber membranes, *J. Membr. Sci.* 382 (1) (2011) 116–123.
- [35] P. Sukitpaneeit, T.-S. Chung, High performance thin-film composite forward osmosis hollow fiber membranes with macrovoid-free and highly porous structure for sustainable water production, *Environ. Sci. Technol.* 46 (13) (2012) 7358–7365.
- [36] J. Ren, J.R. McCutcheon, Polyacrylonitrile supported thin film composite hollow fiber membranes for forward osmosis, *Desalination* 372 (2015) 67–74.
- [37] M. Shibuya, et al., A thin-film composite-hollow fiber forward osmosis membrane with a polyketone hollow fiber membrane as a support, *Desalination* 402 (2017) 33–41.
- [38] K. Zheng, S. Zhou, X. Zhou, High-performance thin-film composite forward osmosis membrane fabricated on low-cost PVB/PVC substrate, *N. J. Chem.* 42 (16) (2018) 13382–13392.
- [39] A. Behboudi, Y. Jafarzadeh, R. Yegani, Polyvinyl chloride/polycarbonate blend ultrafiltration membranes for water treatment, *J. Membr. Sci.* 534 (2017) 18–24.
- [40] C.F. Wan, T.-S. Chung, Osmotic power generation by pressure retarded osmosis using seawater brine as the draw solution and wastewater retentate as the feed, *J. Membr. Sci.* 479 (2015) 148–158.
- [41] S. Zhang, P. Sukitpaneeit, T.-S. Chung, Design of robust hollow fiber membranes with high power density for osmotic energy production, *Chem. Eng. J.* 241 (2014) 457–465.
- [42] A.K. Ghosh, et al., Impacts of reaction and curing conditions on polyamide composite reverse osmosis membrane properties, *J. Membr. Sci.* 311 (1–2) (2008) 34–45.
- [43] P.J. Flory, Fundamental principles of condensation polymerization, *Chem. Rev.* 39 (1) (1946) 137–197.
- [44] A. Soroush, et al., Interfacially polymerized polyamide thin film composite membranes: Preparation, characterization and performance evaluation, *Desalination* 287 (2012) 310–316.
- [45] Alihemati, Z., et al., *Feasibility of using polycarbonate as a substrate of thin film composite membrane in forward osmosis*. *Journal of Applied Polymer Science*: p. 50511.
- [46] H. Ahmadi, S. Hashemifard, A. Ismail, A research on CO₂ removal via hollow fiber membrane contactor: The effect of heat treatment, *Chem. Eng. Res. Des.* 120 (2017) 218–230.
- [47] S. Sahebi, et al., Effect of sulphonated polyethersulfone substrate for thin film composite forward osmosis membrane, *Desalination* 389 (2016) 129–136.
- [48] D. Wang, K. Li, W. Teo, Effects of temperature and pressure on gas permselectivity properties in asymmetric membranes, *J. Membr. Sci.* 105 (1–2) (1995) 89–101.
- [49] Hashemifard, S., et al., *A novel approach to predict the skin layer porosity of porous asymmetric membranes via gas permeation test*. *Chemical Engineering Research and Design*, 2020.
- [50] S. Hashemifard, T. Matsuura, A. Ismail, Predicting the rarefied gas flow through circular nano/micro short tubes: A semi-empirical model, *Vacuum* 164 (2019) 18–28.
- [51] L. Jin, et al., Polyamide-crosslinked graphene oxide membrane for forward osmosis, *J. Membr. Sci.* 545 (2018) 11–18.
- [52] A. Shakeri, et al., Polyoxometalate based thin film nanocomposite forward osmosis membrane: Superhydrophilic, anti-fouling, and high water permeable, *J. Colloid Interface Sci.* 536 (2019) 328–338.
- [53] X. Xu, et al., Conductive thin film nanocomposite forward osmosis membrane (TFN-FO) blended with carbon nanoparticles for membrane fouling control, *Sci. Total Environ.* 697 (2019), 134050.
- [54] D. Xiao, et al., A modeling investigation on optimizing the design of forward osmosis hollow fiber modules, *J. Membr. Sci.* 392 (2012) 76–87.
- [55] F. Lipnizki, R.W. Field, Mass transfer performance for hollow fibre modules with shell-side axial feed flow: using an engineering approach to develop a framework, *J. Membr. Sci.* 193 (2) (2001) 195–208.
- [56] D.B. Marghitu, *Mechanical engineer's handbook*, Elsevier, 2001.
- [57] A. Charfi, N.B. Amar, J. Harmand, Analysis of fouling mechanisms in anaerobic membrane bioreactors, *Water Res.* 46 (8) (2012) 2637–2650.

- [58] G. Bolton, D. LaCasse, R. Kuriyel, Combined models of membrane fouling: development and application to microfiltration and ultrafiltration of biological fluids, *J. Membr. Sci.* 277 (1–2) (2006) 75–84.
- [59] R. Jiraratananon, A. Chanachai, A study of fouling in the ultrafiltration of passion fruit juice, *J. Membr. Sci.* 111 (1) (1996) 39–48.
- [60] M. Khayet, et al., Structural and performance studies of poly (vinyl chloride) hollow fiber membranes prepared at different air gap lengths, *J. Membr. Sci.* 330 (1–2) (2009) 30–39.
- [61] M. Khayet, The effects of air gap length on the internal and external morphology of hollow fiber membranes, *Chem. Eng. Sci.* 58 (14) (2003) 3091–3104.
- [62] Q. She, X. Jin, C.Y. Tang, Osmotic power production from salinity gradient resource by pressure retarded osmosis: Effects of operating conditions and reverse solute diffusion, *J. Membr. Sci.* 401 (2012) 262–273.
- [63] K.Y. Wang, T.-S. Chung, J.-J. Qin, Polybenzimidazole (PBI) nanofiltration hollow fiber membranes applied in forward osmosis process, *J. Membr. Sci.* 300 (1–2) (2007) 6–12.
- [64] M. Shibuya, et al., Effects of operating conditions and membrane structures on the performance of hollow fiber forward osmosis membranes in pressure assisted osmosis, *Desalination* 365 (2015) 381–388.
- [65] T. Majeed, et al., Influence of the process parameters on hollow fiber-forward osmosis membrane performances, *Desalin. Water Treat.* 54 (4–5) (2015) 817–828.
- [66] J. Ren, J.R. McCutcheon, A new commercial biomimetic hollow fiber membrane for forward osmosis, *Desalination* 442 (2018) 44–50.
- [67] Y. Yabuno, et al., Preparation of polyamide thin-film composite membranes using hydrophilic hollow fiber PVDF via the TIPS process modified by PVA diffusion, *Ind. Eng. Chem. Res.* 58 (47) (2019) 21691–21699.
- [68] G. Di Bella, D. Di Trapani, A brief review on the resistance-in-series model in membrane bioreactors (MBRs, *Membranes* 9 (2) (2019) 24.
- [69] S. Lee, et al., Comparison of fouling behavior in forward osmosis (FO) and reverse osmosis (RO), *J. Membr. Sci.* 365 (1–2) (2010) 34–39.
- [70] J. Ren, et al., A computational fluid dynamics model to predict performance of hollow fiber membrane modules in forward osmosis, *J. Membr. Sci.* 603 (2020), 117973.